



Cite this: *J. Mater. Chem. C*, 2019,  
7, 14913

## A novel 3D-printable hydrogel with high mechanical strength and shape memory properties†

Qiang Zhou, Kaixiang Yang, Jiaqing He, Haiyang Yang \* and Xingyuan Zhang \*

The three-dimensional (3D)-printing of hydrogels with excellent mechanical properties has attracted extensive attention owing to their potential applications in many fields. Through the photoinitiated copolymerization of methacrylic acid (MAAc) and *N*-(pyridin-2-yl)acrylamide (NPAM) in dimethylsulfoxide (DMSO), a copolymer solution was prepared; it was then 3D printed at 70 °C followed by solvent replacement of DMSO with water at 25 °C, and a novel 3D-printed tough hydrogel was prepared. In the presence of water, NPAM could undergo “multi-fold” hydrogen bonding with MAAc. Thus, the hydrogen bonding is strengthened and stabilized by the hydrophobic  $\alpha$ -methyl of MAAc and the pyridine N-heterocycle of NPAM, meaning that the modules of the hydrogel can be up to five times stronger than the original organogels. The swelling or shrinkage of the gel is negligible during solvent replacement and the resultant hydrogel exhibits excellent mechanical properties, with an elastic modulus of 1.8–66 MPa, a tensile fracture stress of 2.2–6.3 MPa, a fracture strain of 360–570% and a fracture energy of 0.5–7.2 kJ m<sup>-2</sup>. In addition, owing to the dynamic nature and temperature sensitivity of the hydrogen bonds, the hydrogel also exhibited fast self-recovery abilities and temperature activated shape memory properties. In particular, the hydrogen-bonding hydrogel could be quickly degraded and recovered by adjusting the pH, which allowed convenient recycling of the hydrogels. Our experimental results indicated that the combination of a 3D-printing technique and solvent replacement may provide a novel and effective method to obtain 3D-printed hydrogels with high mechanical strength and shape recovery properties, fostering their use in a number of fields such as soft robots, implant devices, tissue engineering and other environment friendly materials.

Received 7th September 2019,  
Accepted 28th October 2019

DOI: 10.1039/c9tc04945b

rsc.li/materials-c

## Introduction

Hydrogels are a kind of hydrated, three-dimensional network structural material that display a variety of desirable properties for engineering applications including for use in actuators,<sup>1,2</sup> smart sensors,<sup>3,4</sup> implant devices<sup>5</sup> and for tissue engineering.<sup>6</sup> However, they are limited by the traditional manufacturing processes, as it is difficult to fabricate hydrogels into complex shapes and multi-material devices. Meanwhile, three-dimensional (3D) printing, also referred to as additive manufacturing (AM), which does not require molds, employs digital designs to fabricate complex 3D objects on demand. 3D printing has been used in many fields including tissue engineering,<sup>7,8</sup> electronics devices,<sup>9</sup> microfluidics,<sup>10</sup> high specific strength materials,<sup>11</sup> and microbiology.<sup>12</sup> Combining hydrogels with 3D-printing has

become a new trend and several printing methods have been developed in the past few years, such as stereolithography technology,<sup>13</sup> the two-photon polymerization microfabrication method,<sup>14,15</sup> and extrusion 3D printing.<sup>16–20</sup> Among these methods, extrusion printing is suitable for viscoelastic materials, and is the method most easily applied to multi-material printing at high resolution and low costs.<sup>21–23</sup>

Extrusion 3D printing is a layer-by-layer assembly methodology in which ink is in a liquid state during extrusion and “frozen” to a solid state after extrusion. As for the hydrogels, because of their poor stability in high temperature ranges, using the differences in the viscosity properties at different temperature to fabricate 3D-printing hydrogels is limited. Therefore, various kinds of gelation mechanisms have been designed to develop tough hydrogel 3D printing techniques. For example, Zhang *et al.* developed a 3D printing strategy relying on the distinct strength of the ionic bonding in polyisocyanopeptide (PIC) hydrogels at different stages of printing, and the printed PIC structures possessed excellent mechanical properties in terms of the extensibility, strength, and toughness.<sup>24</sup> By using nanoclay to control

CAS Key Laboratory of Soft Matter Chemistry, School of Chemistry and Materials Science, University of Science and Technology of China, Hefei, 230026, P. R. China.  
E-mail: yhy@ustc.edu.cn, zxy@ustc.edu.cn

† Electronic supplementary information (ESI) available. See DOI: 10.1039/c9tc04945b

the viscosity of the pre-gel solution, Zhao and his co-workers<sup>25</sup> created a 3D-printable tough PEG-alginate–nanoclay hydrogel which had a fracture toughness as high as  $1500 \text{ J m}^{-2}$ . Wu *et al.* used highly viscoelastic double-network SA/AAm/AAc solutions to print 3D constructs, then the printed hydrogels were polymerized under UV irradiation and transferred into a  $\text{FeCl}_3$  solution for further fixation by forming robust carboxyl- $\text{Fe}^{3+}$  coordination complexes.<sup>20</sup> By subtly avoiding the negative effects of high temperature on hydrogel viscosity, these 3D-printing hydrogels exhibit great mechanical properties and 3D-printing processability. However, many difficulties still exist, such as volume swelling during shape fixation and short storage life in air, unless additional multi-component containers and complex devices are introduced.

In order to overcome the shortcomings mentioned above, here we demonstrate a novel 3D-printable tough hydrogel and a novel two-step strategy to fabricate it. First, we prepared an organogel ink facilely by photoinitiated copolymerization of methacrylic acid (MAAc) and *N*-(pyridin-2-yl)acrylamide (NPAM) in dimethylsulfoxide (DMSO) and then extruded it to fabricate 3D-printed organogels. The organogel could be extruded at  $70^\circ\text{C}$  and molded at  $25^\circ\text{C}$ , which is suitable for extrusion printing. In addition, the organogel benefited from the high boiling point of DMSO, and was found to be stable long-term at room temperature in air compared to the hydrogels. Secondly, the obtained organogel was immersed in deionized water to form a tough hydrogel. Owing to the form of the hydrophobic interaction that stabilized the hydrogen bonds, the gel was resistant to swelling throughout the dialysis and retained its original morphology. In the meantime, the temperature sensitivity of the hydrogen bonding endowed the hydrogels with shape memory behavior, which provided potential capabilities for 4D printing.<sup>26,27</sup>

As for the bulk hydrogels, the form of hydrogen bonding and further stabilization by the hydrophobic interactions endowed them with excellent mechanical properties, with an elastic modulus of  $1.8\text{--}66 \text{ MPa}$ , a tensile fracture stress of  $2.2\text{--}6.3 \text{ MPa}$ , a fracture strain of  $360\text{--}570\%$  and a toughness of  $0.5\text{--}7.2 \text{ kJ m}^{-2}$ . Although there are no chemical cross-linkers in the hydrogel, the mechanical properties are still superior to most existing hydrogels and comparable to tough soft biotissues, especially according to the modulus.<sup>28–31</sup> Benefiting from the absence of chemical cross-linkers, through protonation and deprotonation of the functional groups under strong acid or alkaline environments, the hydrogen-bonding hydrogel could quickly degrade and be recovered by adjusting the pH. This property makes recycling of the hydrogels efficient and convenient. To the best of our knowledge, this kind of 3D printed hydrogel with these excellent mechanical properties and novel fabricating strategy has rarely been reported.

## Experimental

### Materials

2-Aminopyridine, acryloyl chloride, 2-hydroxy-4'-(2-hydroxyethoxy)-2-methylpropiophenone (IRGACURE 2959) was purchased from Sigma-Aldrich. MAAc, acrylic acid (AAc), triethylamine (TEA), urea, sodium hydroxide (NaOH) and hydrochloric acid (HCl) was

purchased from the Shanghai Institute of Cell Biology (Shanghai, China). Dichloromethane, DMSO and ethyl acetate were purchased from Energy Chemical.

### Synthesis and NMR characterization of *N*-(pyridin-2-yl)acrylamide

*N*-(Pyridin-2-yl)acrylamide was synthesized according to a previously reported literature method.<sup>32</sup> Acryloyl chloride (3.5 g, 36.7 mmol) was dissolved in 100 ml dichloromethane and placed in an ice bath. 2-Aminopyridine (2-AP, 3 g, 31.9 mmol) and triethylamine (3.7 g, 36.7 mmol) were dissolved in dichloromethane (20 ml). TEA was added to neutralize the hydrochloric acid that was formed as a side product of the reaction. The mixture (reagent/triethylamine) was poured dropwise into acryloyl chloride under constant magnetic stirring. In all cases, a yellow viscous solution was obtained after the complete addition of the reagent/TEA mixture. After the addition, the mixture was stirred overnight at room temperature. Once the reaction was completed, the dichloromethane was concentrated using a rotary evaporator. The clear oil obtained was dissolved in distilled water (solution A). Solution A was extracted using ethyl acetate and washed with water three times. The resulting solution was concentrated using a rotary evaporator and dried overnight in a vacuum oven to obtain an orange/red solid (3.1824 g, yield: 52%, the  $^1\text{H}$  NMR spectrum can be seen in Fig. S1, ESI†).

### Preparation of the poly(MAAc-*co*-NPAM) hydrogel

The preparation process of the poly(MAAc-*co*-NPAM) hydrogel is illustrated in Fig. 1a. Firstly, a certain amount of MAAc and NPAM (the total mass was 1 g, of which NPAM accounts for 4 mol%, 6 mol%, 8 mol%, or 10 mol% of the total monomers) and the photoinitiator IRGACURE 2959 (2 mg, 0.5 mol%) were dissolved in 1.2 g DMSO. The resulting solution was poured into a glass mold and polymerized under UV irradiation for 5 h. After polymerization, the hydrogel sample was immersed in a large excess of water at room temperature to replace the DMSO with water.<sup>33,34</sup> The resultant gel sample was named  $\text{MN}_x$ , in which  $x$  represented the molar fraction of NPAM in the total monomer. In addition, the  $\text{AN}_x$  gel was prepared using the same molar amount of AAc instead of MAAc, the other conditions were unchanged.

### Characterization of hydrogels

Fourier-transform infrared spectroscopy (FTIR) spectra (Nicolet 8700 FTIR, USA) was used to characterize the dry hydrogel samples. A comparative sample of polymethacrylic acid (PMAAc) powder was obtained by the photoinitiated copolymerization of MAAc (1 M) in aqueous solution followed by lyophilization. Poly(2-acrylamidopyridine) (PNPAM) powder was obtained through photoinitiated copolymerization in tetrahydrofuran, and followed by precipitation in isopropanol and vacuum drying.

### Water content test

The water contents of the hydrogels were measured using the weight change upon vacuum freeze dehydration. The water content  $C$  (wt%) is defined by the weight of hydrogels after

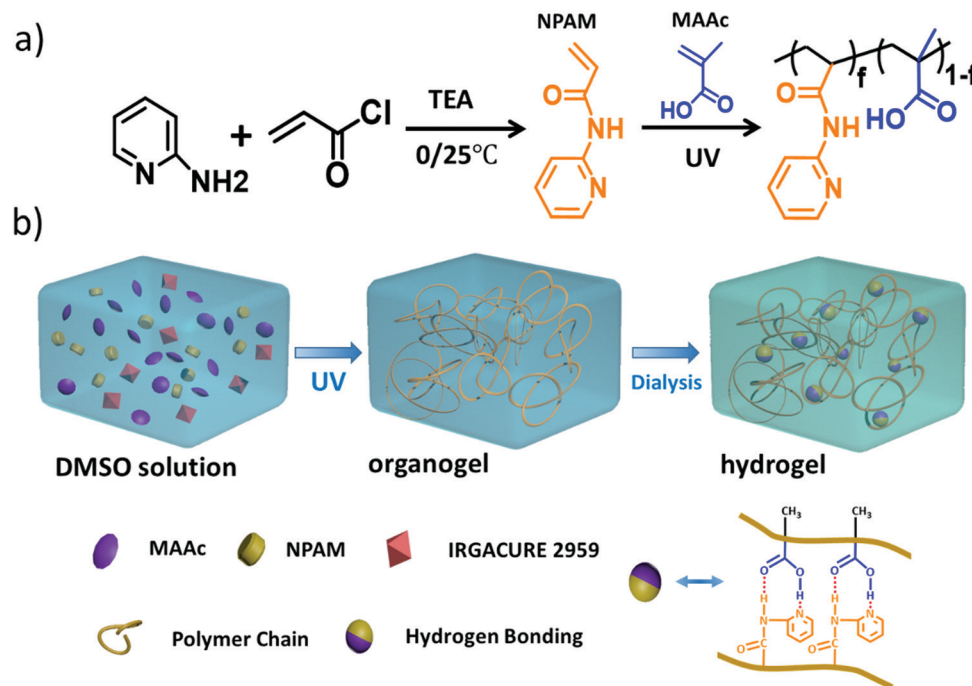


**Fig. 1** The preparation process (a) and formation mechanism (b) of the poly(MAAc-*co*-NPAM) hydrogel.

lyophilization ( $W_1$ ) and the total weight of the hydrogels before lyophilization ( $W_0$ ).

$$C \text{ (wt)} = \frac{W_0 - W_1}{W_0} \times 100\% \quad (1)$$

The swelling ratios of the hydrogels were measured using the weight change upon swelling in various solutions for 120 h at room temperature. The swelling ratio  $S$  is defined as the ratio of the weight of the hydrogels after swelling ( $M_1$ ) to the weight of the hydrogels before swelling ( $M_0$ ).

$$S \text{ (g g}^{-1}\text{)} = \frac{M_1}{M_0} \quad (2)$$

### 3D printing of organogels

A 3D printing system was customized to print the organogel structures. There are two parts to the 3D printing system: an extrusion-based dispersion system and a 3D positioning stage (Fig. 1). The extrusion system consists of an air pump, a pressure controller, and heated syringes with temperature control. During the printing process, the organogel was heated to 70 °C in an iron syringe and pneumatically extruded into a glass plate at room temperature, where the organogel gelated into a solid gel rapidly. Then, the organogel was soaked in deionized water for more than 5 d for it to change itself into a hydrogel.

The printed organogels and the swelled hydrogels were photographed using the digital camera or optical microscope. The corresponding CAD files have been included in the ESI.†

### Mechanical tests

The mechanical properties of hydrogels were all tested on an electronic universal testing machine (EZTest, SHIMADZU) at

room temperature. For the tensile and loading-unloading tests, the hydrogel samples were extruded to a cylinder shape with a radius of 2 mm. In the loading-unloading tests, in order to prevent the water evaporating, all of the samples were coated with silicone oil. In the cyclic tests, all hydrogel samples were kept in water to avoid water evaporation after the long testing period. The crosshead velocity was fixed at 120 mm min<sup>-1</sup>, unless otherwise noted. All of the stresses measured were engineering stresses or nominal stresses, the Young's moduli were calculated from the slope of the stress-strain curves between the 1% and 5% stains and the toughness was calculated from the entire area of the stress-strain curves. The dissipative energy was calculated from the integral area of the hysteretic circle of the extension-recovery curve.

For the tearing test, the hydrogel samples were cut into a trouser shape according to GBT 529-2008 A standard (1/2 sized, width: 7.5 mm, length: 50 mm, notch length: 20 mm, and thickness: 1.2 mm). The two legs of the test sample were clamped and the crosshead velocity was 240 mm min<sup>-1</sup>. The tearing energy  $T$  was calculated using the formula:

$$T = F/d \quad (3)$$

in which  $F$  is the average force during the tear and  $d$  is the thickness of the sample.

### Rheological measurements

The rheological behavior of the hydrogels was characterized with a rheometer (TA AR-G2, TA Instruments) equipped with 40 mm parallel plates. A solvent trap was filled with silicone oil to minimize water evaporation. Frequency sweeps were performed at different temperatures at 0.1% strain. The storage modulus ( $G'$ ) and the

loss modulus ( $G''$ ) were measured as a function of the angular frequency from 0.01 to 100 Hz. The master curves of the storage modulus  $G'$  and loss modulus  $G''$  were obtained using the time-temperature superposition shifts (TTS) at the 40 °C reference temperature. The temperature was increased stepwise from low to high and the sample was held at the set temperature for 300 s to reach equilibrium at each measurement. On the basis of the Arrhenius plot of the temperature-dependent shift factors, the apparent activation energy  $E_a$  was calculated from the slope of the curve. Temperature sweep data were obtained at a fixed frequency ( $\omega = 6.2 \text{ rad s}^{-1}$ ) and strain ( $\gamma = 0.5\%$ ) covering a range of 10–60–10 °C (heating and cooling rate: 2 °C min<sup>-1</sup>).

### Shape memory behavior

The  $\text{MN}_6$  hydrogel sample with a simple flower shape was deformed into a state of collapse at 60 °C. The temporary shape was fixed at 10 °C for 2 min. When the deformed gel was immersed in 60 °C deionized water again, the shape quickly recovered to the original flower shape within 70 s. The cylindrical hydrogel  $\text{MN}_6$  sample with an initial spiral shape was deformed into a straight shape at 60 °C for 2 min. The temporary shape was fixed at 10 °C for another 2 min. The sample was then transferred into a hot water bath of 60 °C to recover its initial shape. The shape fixity ratio ( $R_f$ ) and shape recovery ratio ( $R_r$ ) were defined using the following equations:  $R_f = \theta_t/\theta_i \times 100\%$ ,  $R_r = (\theta_i - \theta_f)/\theta_i \times 100\%$ , in which  $\theta_i$  is the given angle,  $\theta_t$  is the temporarily fixed angle, and  $\theta_f$  is the final angle.

## Results and discussion

### Formation and structural characterization of the poly(MAAC-co-NPAM) hydrogel

The preparation process and formation mechanism of the poly(MAAC-co-NPAM) hydrogel are illustrated in Fig. 1a and b. We used a two-step method to synthesize the poly(MAAC-co-NPAM) hydrogel. First, the monomer NPAM was synthesized by amidation of *N*-(pyridin-2-yl)acrylamide and acryloyl chloride. Then, the monomers of NPAM and MAAC were polymerized under UV irradiation to form the homogeneous poly(MAAC-co-NPAM) organogel. In the second step, the organogel was immersed in deionized water to replace the DMSO, converting the organogel into a hydrogel. The hydrogel could be cross-linked by the intermolecular hydrogen bonds between the NPAM and carboxylic acid groups. In order to verify the intermolecular hydrogen bonding between the NPAM and carboxylic acid groups, FTIR spectra of different samples were measured. As shown in Fig. 2a, the characteristic peak, C=N (C=N (ring) stretching mode), shifted from 1524 cm<sup>-1</sup> in the spectrum of the PNPAM hydrogel to 1537 cm<sup>-1</sup> in the spectrum of the poly(MAAC-co-NPAM<sub>20</sub>) hydrogel. In addition, the peak at 1714 cm<sup>-1</sup> in the spectrum of the PMAAc hydrogel ascribed to the C=O stretching vibration of the carboxylic acid group shifted to 1703 cm<sup>-1</sup> in the spectrum of the poly(MAAC-co-NPAM<sub>20</sub>) hydrogel.<sup>35,36</sup> These results indicated the formation of hydrogen bonds between the carboxylic acid and pyridine groups.<sup>37,38</sup> To further verify the formation of

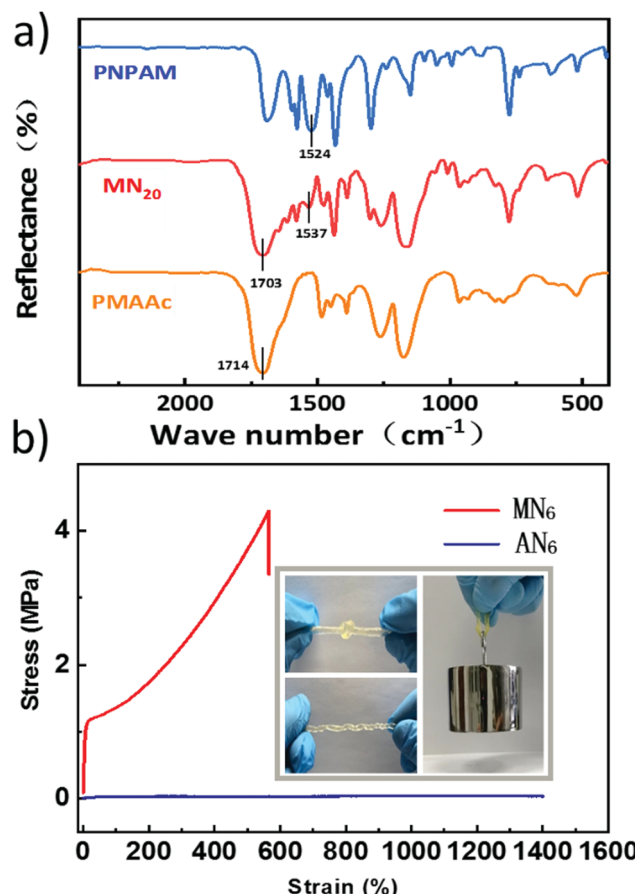


Fig. 2 (a) FTIR spectra of the PNPAM hydrogel,  $\text{MN}_{20}$  hydrogel, and PMAAc hydrogel. (b) The tensile stress–strain ( $\sigma_t$ – $\epsilon_t$ ) curves of the  $\text{MN}_6$  hydrogel and  $\text{AN}_6$  hydrogel; the inset shows the knotted and twisted  $\text{MN}_6$  hydrogel cylinder (radius of 2.6 mm) as it lifts up a steel block 1 kg in weight.

hydrogen bonds cross-linked between the molecular chains, the  $\text{MN}_{10}$  hydrogel was immersed in 5 M urea (a typical hydrogen-bonding disrupter) solution at room temperature, as shown in Fig. S2 (ESI<sup>†</sup>). The gel was completely dissolved in the urea solution after 8 d. In contrast, the  $\text{MN}_{10}$  hydrogel remained intact in deionized water after 8 d, which indicated that the hydrogels were only linked by hydrogen bonds.

In previous studies, hydrophobic interactions were introduced to strengthen the hydrogen-bonding domains.<sup>39–41</sup> Accordingly, Fig. S3 (ESI<sup>†</sup>) shows that the NPAM solutions appeared to form an apparently water-insoluble blend after the addition of MAAC, which will gradually dissolve in water with the addition of urea. In contrast, adding AAc into the NPAM solution did not induce macroscopic phase separation, probably because hydrophobic interactions between the hydrophobic  $\alpha$ -methyl moieties of the MAAC and pyridine N-heterocycle of NPAM facilitated the formation of multiple hydrogen-bonding interactions between MAAC and NPAM. Furthermore, we synthesized an  $\text{AN}_6$  hydrogel by replacing MAAC with AAc, a more hydrophilic monomer. As shown in Fig. 2b, the mechanical strength of the  $\text{MN}_6$  hydrogel was much higher than that of the  $\text{AN}_6$  hydrogel. The  $\text{MN}_6$  hydrogel sheet with a diameter of 2 mm could still lift a heavy

steel block with a 1 kg weight after being twisted and knotted. However, the  $\text{AN}_6$  hydrogel was too weak to achieve this. It also proved that the hydrophobic interactions facilitated the formation of strong hydrogen-bonding domains.

### 3D printing processability

In the process of preparing hydrogels, we found the organogel exhibited significant differences in the rheological properties at different temperatures. Whether gels are suitable for extrusion printing is closely related to the viscosity properties of the gel.<sup>42</sup> Therefore we performed further rheological tests on the organogels. From the rheological behaviors of the  $\text{MN}_6$  gel shown in Fig. 3c, we observed that the loss modulus  $G''$  of the organogel was larger than the storage modulus  $G'$  in all frequency ranges at 70 °C, which indicated that the organogels were easy to extrude at 70 °C. At 25 °C, the loss modulus  $G''$  of the organogel was smaller than the storage modulus  $G'$  in all frequency ranges, which was beneficial to the molding of the organogels after extrusion.

In addition, we found that the gels feature swelling resistance upon water immersion. The appearance of both the organogels and equilibrated hydrogels with different molar fractions of NPAM are shown in Fig. 3a and b. All of the organogel samples were cut into 2 cm diameter discs. When the organogels were transformed into hydrogels, the poly(MAAc-*co*-NPAM<sub>*X*</sub>) hydrogel swelled a lot but the others swelled a little. The swelling ratios of the poly(MAAc-*co*-NPAM<sub>*X*</sub>) hydrogels were measured. The equilibrium water content (EWC) and volume expansion of the poly(MAAc-*co*-NPAM<sub>*X*</sub>) hydrogels are listed in Table 1. The volume expansion of the hydrogels decreased from 1.42 to 1.03 with the increasing molar fraction of NPAM. It is noted that the  $\text{MN}_X$  ( $X = 6, 8, 10$ ) hydrogel maintains its original shape and performance for more than 15 d under an aqueous environment.

Meanwhile, we also observed that the storage modulus  $G'$  of the hydrogel was more than 20 times larger than the organogel at 25 °C after it had been immersed in water to replace the DMSO with water. Similar situations also occurred in the  $\text{MN}_8$  and  $\text{MN}_{10}$  gels (Fig. S4, ESI†). Judging from the rheological properties of the organogels and the excellent swelling resistance of the hydrogels, we developed a novel type of 3D printed tough hydrogel.

In order to fabricate a tough 3D-printed hydrogel, a two-step method was used as shown in Fig. 4. The organogel was first extruded from a 70 °C environment onto a glass plate at 25 °C. A video (Movie S1) has been included in the ESI† to show the first printing process. Then, after the printing process, the obtained organogel was immersed in water to change itself into a hydrogel. Using this novel two-step method, we successfully fabricated many 3D-printed hydrogels. Fig. 5a and c show the top and side view of a 4-layered grid (fiber diameter, 0.8 mm; spacing, 0.6 mm) of the  $\text{MN}_6$  hydrogel, respectively, and the respective microphotograph is exhibited in Fig. 5b and d. We also exhibited the top view of the corresponding organogel (see Fig. S5a and b, ESI†). From these pictures we can see that the construction of the gel grid does not undergo any changes after dialysis, in either the microscopic images or macroscopic photos. This shows that the final gel structure can be effectively controlled using the two-step method. On the basis of these cases,

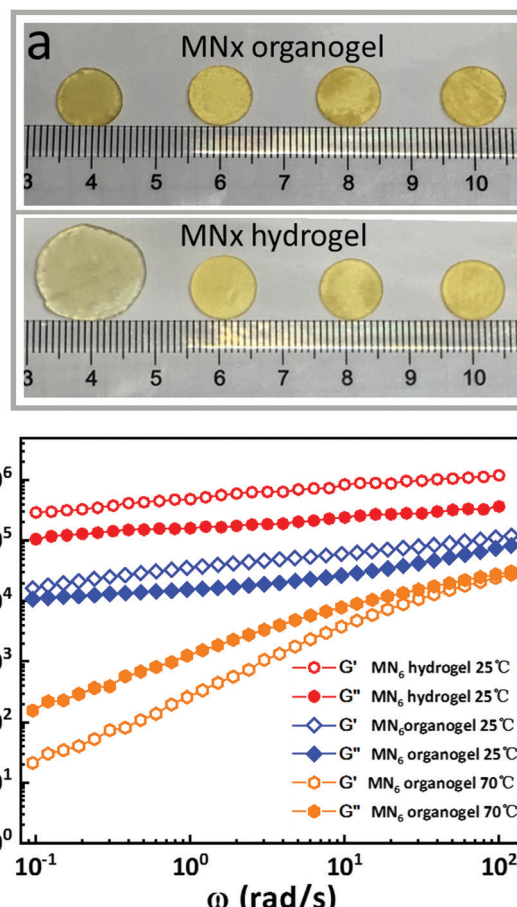
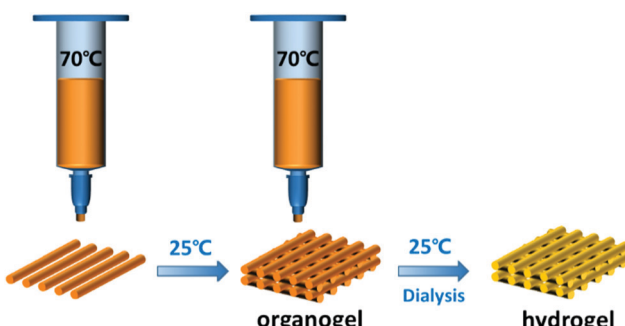


Fig. 3 (a) The swelling behaviour, showing how the  $\text{MN}_x$  organogels convert to hydrogels (from left to right,  $x = 4, 6, 8, 10$ ). (b) Temperature-dependent viscoelastic behavior curves for the  $\text{MN}_6$  hydrogels and organogels;  $\gamma = 0.5\%$ .

Table 1 Equilibrium water content of the poly(MAAc-*co*-NPAM<sub>*X*</sub>) hydrogels

Hydrogel sample	EWC (wt%)	Volume expansion
Poly(MAAc- <i>co</i> -NPAM <sub>4</sub> ) ( $\text{MN}_4$ )	$70.3 \pm 2.3$	1.42
Poly(MAAc- <i>co</i> -NPAM <sub>6</sub> ) ( $\text{MN}_6$ )	$58.2 \pm 1.5$	1.17
Poly(MAAc- <i>co</i> -NPAM <sub>8</sub> ) ( $\text{MN}_8$ )	$53.6 \pm 1.6$	1.08
Poly(MAAc- <i>co</i> -NPAM <sub>10</sub> ) ( $\text{MN}_{10}$ )	$51.2 \pm 1.3$	1.03

various complex structures can be constructed using the 3D printing technology. Fig. 5e and f show a triangular prism and a simple flower made from  $\text{MN}_6$  gels, respectively. In Fig. S5c (ESI†), we fabricated a 3D-printing arch bridge with a thickness of 1 cm. We can clearly see from the picture that the arch bridge had a high modulus that could bear a steel block of 1 kg in weight. We conducted further research on the mechanical properties of the 3D-printed hydrogel. As shown in Fig. 5g, the tensile fracture stress of the  $\text{MN}_6$  hydrogel grid was 0.44 MPa, which was found to be 20 times higher than the  $\text{MN}_6$  organogel grid. The elastic modulus of the hydrogel grid was 2.64 MPa, which was 50 times higher than the  $\text{MN}_6$  organogel grid. These showed that the swelling resistance of the gel and the good mechanical properties of the hydrogel endows the gel with potential application prospects.



**Fig. 4** The printing process for a two-step method and the corresponding phase: the organogel is first loaded into the iron syringe, heated to 25 °C and pneumatically extruded onto a glass plate at a temperature of 25 °C. After gel formation and stable mechanical properties are achieved, the organogels are soaked in deionized water for more than 5 d to change into hydrogels.

### Mechanical properties

In order to further study the mechanical properties of the gel, we performed many tests on the bulk gel samples, which were extruded into a cylinder shape with a radius of 2 mm. The tensile stress-strain curves, fracture strength and elastic modulus of the poly(MAAc-*co*-NPAM<sub>X</sub>) hydrogels are shown in Fig. 6. The

poly(MAAc-*co*-NPAM<sub>X</sub>) hydrogels exhibited excellent and tunable mechanical properties. With the increase of the NPAM molar ratio, the tensile fracture stress and elastic modulus increased remarkably from 2.2 to 6.3 MPa and from 1.8 to 66 MPa, respectively. The hydrogel elastic modulus increased significantly with the increase of the NPAM content, which results from the increase of the MAAc-NPAM hydrogen bond cross-linking point. The tensile fracture stress and elastic modulus of the organogels were more than two or five orders of magnitude lower than those of the hydrogels, respectively (see the inset in Fig. S6a, ESI<sup>†</sup>), which further demonstrated the significant role of the hydrogen bond in promoting the strength of the hydrogels. However, when the NPAM mole fraction exceeded 8%, the excessively high crosslink density not only led to a decrease in the elasticity, but also resulted in a decrease in the breaking strength and elongation of the hydrogel. In addition to its high strength, these hydrogels had good toughness. As shown in Fig. S6b (ESI<sup>†</sup>), the fracture energy of the hydrogels could reach 7 kJ m<sup>-2</sup>, close to some rubbers and living tissues.<sup>30</sup> In summary, benefiting from the hydrogen bond between NPAM and MAAc and the protection of the hydrophobic interactions, the mechanical properties of these hydrogels were found to be outstanding and could be tuned over wide ranges.

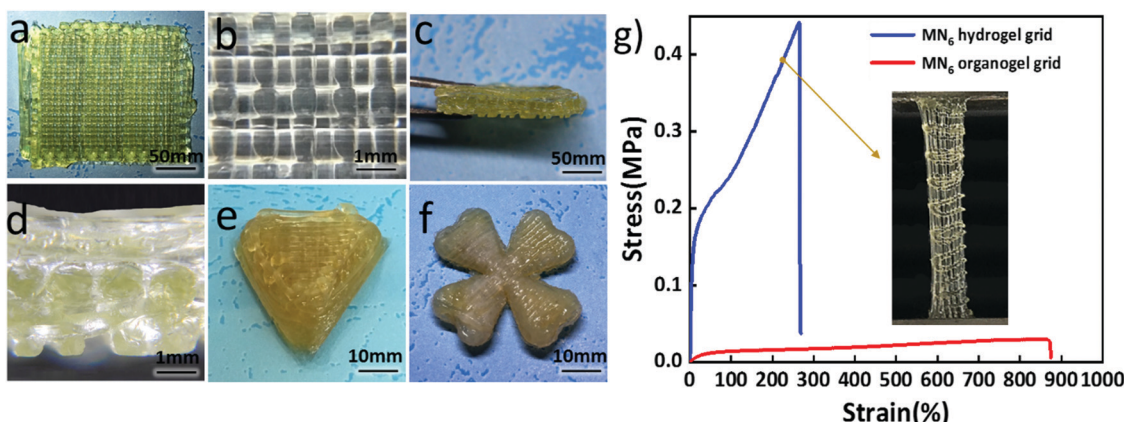


**Fig. 5** (a) Top view, (c) side view, and (b) and (d) the respective microphotographs of a 3D-printed 4-layer grid of the MN<sub>6</sub> hydrogel. The 3D-printed MN<sub>6</sub> hydrogel with (e) a triangular prism shape and (f) a simple flower shape. (g) The tensile stress–strain curves of a 4-layer grid of the MN<sub>6</sub> hydrogels; the inset shows the tensile tests of the MN<sub>6</sub> hydrogel grid when the stress was 0.4 MPa.

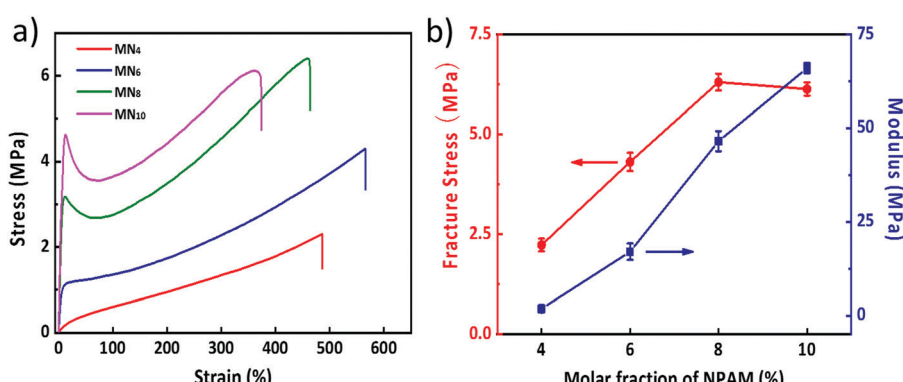


**Fig. 6** (a) Tensile stress–strain curves and (b) tensile fracture stress and elastic modulus data of the MN<sub>4</sub>, MN<sub>6</sub>, MN<sub>8</sub> and MN<sub>10</sub> hydrogels.

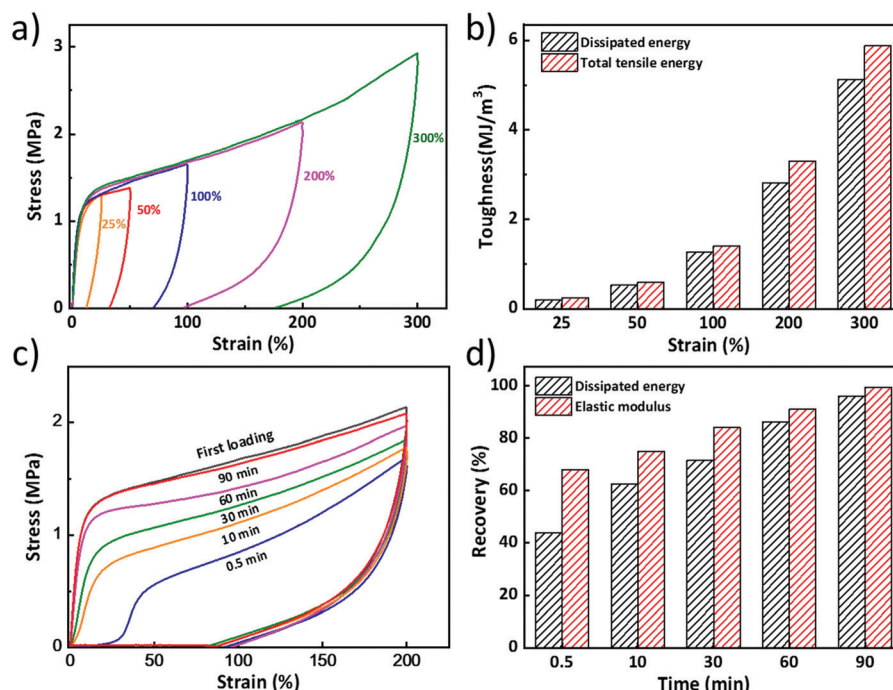


**Fig. 7** (a) Tensile-recovery curves and (b) the total energy and dissipated energies of MN<sub>6</sub> gel samples at different tensile strains (25%, 50%, 100%, 200%, and 300%). (c) The stretch-recovery curves of MN<sub>6</sub> gel samples at different recovery times after 200% strain stretching and (d) the elastic modulus values from the stretch-recovery curves and the recovery ratios from the hysteresis loop areas.

To gain further insights into the internal fracture mechanism of the hydrogels, successive loading–unloading tests were conducted. Fig. 7a shows the loading–unloading curves of the MN<sub>6</sub> hydrogel at different strains. Apparent hysteresis loops and transient residual strains were observed in the loading–unloading curves. The hydrogel had a total tensile energy of 0.25 MJ m<sup>-3</sup> and an energy dissipation of 0.2 MJ m<sup>-3</sup> at 25% strain. When the tensile strain was further increased to 300%, the hydrogel demonstrated a larger hysteresis loop, the total tensile energy reached 5.8 MJ m<sup>-3</sup> and the dissipation energy reached 5.2 MJ m<sup>-3</sup> (Fig. 7b). This high energy dissipation suggested substantial breakage of the hydrogen bonds during stretching. In contrast, the recovery of these hydrogen bonds is fast and efficient. As shown in Fig. 7c, we performed a series of self-recovery loading–unloading tests on the MN<sub>6</sub> hydrogel at different waiting times to test the recovery efficiency of the hydrogel. The MN<sub>6</sub> hydrogel showed a large hysteresis circle after the first stretching and there was a residual strain of about 100%. When the external force was removed and the hydrogel recovered at room temperature for about 10 min, the residual strain disappeared and the shape of the hydrogel completely recovered. The mechanical properties of the gel recovered substantially after about 90 min. As shown in Fig. 7d, the elastic modulus and dissipated energy of the hydrogel was restored to 96% after 90 min, which proved that the hydrogel could completely self-recover after a large deformation. Owing to this efficient self-recovery property, the hydrogel also has potential applications as a fatigue-resistant material. As displayed in the cyclic tests performed on the same hydrogel sample (Fig. S7, ESI†), the hysteresis loops remain essentially the same after 12 h, demonstrating the relatively good fatigue-resistant ability of this material.

Owing to the dynamic nature of the hydrogen bonds, the mechanical properties of the poly(MAAc-*co*-NPAM<sub>X</sub>) hydrogels depended on the frequency and temperature. Therefore we further investigated the dynamic properties of the MN<sub>6</sub> hydrogels using rheological measurements. As shown in Fig. 8a, frequency sweeps were performed in the linear region of the strains and temperatures, and the spectra appeared to follow the time-temperature superposition shift (TTS) principle, validating the use of the TTS curve for calculating the activation energy. It was noted that  $G'$  is larger than  $G''$  over the entire frequency range from  $10^{-6}$  to  $10^6$  Hz, indicating that the sample was always in the gel state with predominantly elastic properties. The apparent activation energy  $E_a$  was obtained using the Arrhenius equation:

$$a_T = Ae^{E_a/RT}$$

In which  $a_T$  is the shift factor,  $R$  is the ideal gas constant, and  $A$  is a constant.<sup>43</sup> The Arrhenius plot for the shift factor  $a_T$  of the master curve is shown in Fig. 8b, along with two distinct apparent activation energies,  $E_a = 162.67$  and  $243.71$  kJ mol<sup>-1</sup>. These values were much larger than those obtained for individual hydrogen bonds ( $12\text{--}20$  kJ mol<sup>-1</sup>),<sup>44</sup> indicating the existence of cooperative hydrogen bond clusters. During the stretching, the weaker hydrogen bond clusters were the first to rupture to dissipate energy, followed by rupture of the stronger ones to resist higher levels of deformation. The energy dissipation mechanism of the poly(MAAc-*co*-NPAM) hydrogels is illustrated in Fig. S8 (ESI†). Not only does the dynamic nature of the hydrogen bonds provide the good fatigue-resistant ability and recovery capability, but it also endows the hydrogels with good shape memory performances.

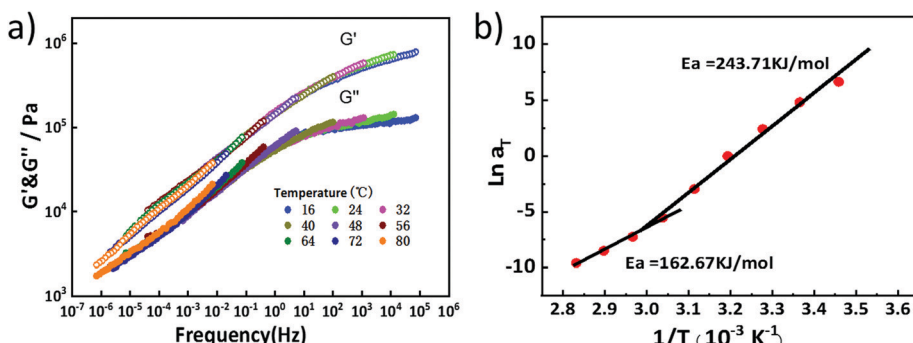


**Fig. 8** Dynamic mechanical behaviour of the  $\text{MN}_6$  hydrogels. (a) The frequency dependence of the storage modulus  $G'$  and loss modulus  $G''$  of the hydrogels. The frequency sweeps were from 0.01 to 100 Hz at a shear strain of 0.1% at different temperatures from 8 to 80 °C; the master curves were obtained using the time-temperature superposition shifts at a reference temperature of 40 °C. (b) An Arrhenius plot for the temperature-dependent shift factors. The apparent activation energy was calculated from the slope of the curve.

### Shape memory performances

The temperature sensitivity of the hydrogen bonds endows the hydrogels with a shape memory ability.<sup>45,46</sup> As shown in Fig. 9a

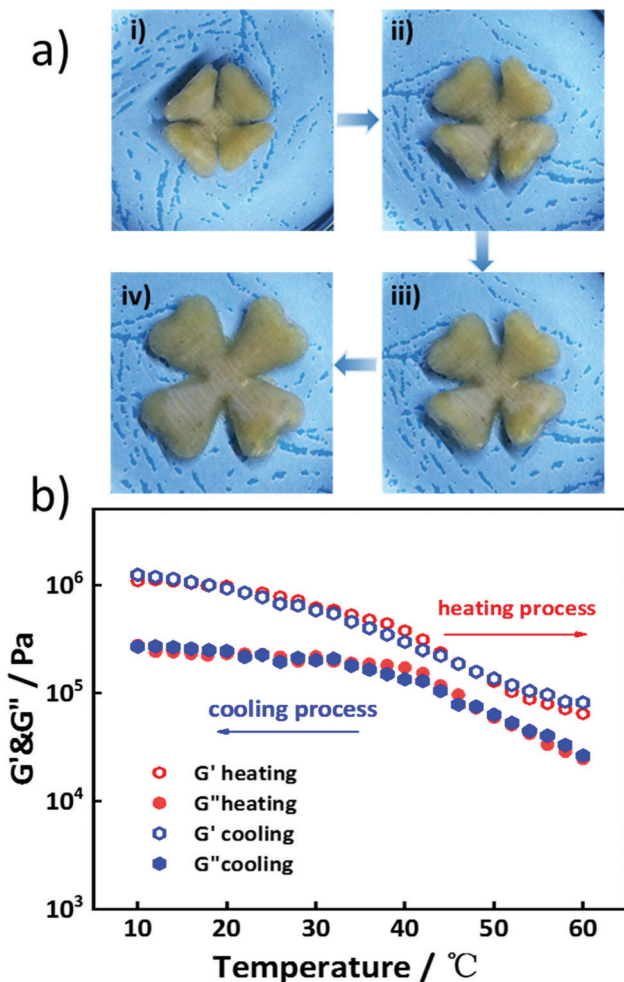


**Fig. 9** (a) The temperature-induced shape memory performance of the 3D-printed  $\text{MN}_6$  hydrogel with a simple flower shape: (i) 0; (ii) 10; (iii) 24; and (iv) 70 s. (b) The viscoelastic behavior curve of the  $\text{MN}_6$  hydrogel during the heating–cooling cycle between 10 and 60 °C.

and Movie S2 (ESI†), the  $\text{MN}_6$  hydrogel sample with a simple flower shape was deformed into a state of collapse at 60 °C. The temporary shape was fixed at 10 °C for 2 min. When the deformed gel was immersed in 60 °C deionized water again, its shape quickly recovered to the original flower shape within 70 s. The mechanism of the shape memory behavior could be manifested by the dynamic mechanical behavior of the hydrogel. A similar temperature-induced shape memory performance with a spiral shape was performed in Fig. S9a and Movie S3 (ESI†).

In order to investigate the reason for the shape memory of the hydrogels, a temperature sweep in terms of the elastic modulus  $G'$  and loss modulus  $G''$  in the range of 10–60–10 °C was performed (Fig. 9b).  $G'$  and  $G''$  of the hydrogel displayed a dramatic temperature dependence in the range of 10–60 °C, and the  $G'$  at 10 °C was more than an order of magnitude higher than that at 60 °C (Fig. S9b, ESI†). The decrease of  $G'$  and  $G''$  with the increase of temperature contributed to the softening nature. Upon cooling,  $G'$  and  $G''$  could return to their original levels, indicative of the reversible tunable mechanical properties of these hydrogels between the hard and soft states. During this progress, the weak hydrogen bonds fractured at high temperature and regenerated at low temperature, which facilitated the fixation of the hydrogel to the deformed shape. When the sample was placed in a high-temperature environment once again, the newly formed weak hydrogen bonds fractured, and the hydrogel recovered to its original shape which was maintained by the strong hydrogen bonding during the entire process.

Furthermore, the shape recovery ratio was measured. In Fig. S10 and Movie S4 (ESI†), images and a video demonstrating the transition from the temporary shape to the permanent shape are shown. A strip sample was heated to 60 °C so that the sample became totally soft and could easily be deformed into a “U” shape, then the temporary shape was fixed upon cooling to 10 °C. Lastly, immersion of the sample in 60 °C water allowed the sample to recover its permanent shape within several seconds. In addition, the shape recovery ratio  $R_f$  measured versus time is presented in Fig. S11a (ESI†). The shape fixity ratio ( $R_f$ ) and shape recovery ratio ( $R_r$ ) were around 100 and 95% (Fig. S11b, tested for five cycles, ESI†), respectively. Therefore, the thermal-activated shape memory performance was easily reproduced.

## Recycling of hydrogels

Owing to the simple structure of the hydrogel and the absence of the cross-linking agent, the hydrogels were expected to have recycling properties through the destruction and reconstruction of the hydrogen bonding. A simple strategy to destroy the hydrogen bonding is the protonation or deprotonation of the monomer by a change in the pH. As shown in Fig. 10a, the fragmented  $\text{MN}_6$  hydrogels were completely dissolved in 0.5 M KOH solution (or 0.1 M HCl solution). After solution casting, the final casted film was swelled in 1 M HCl solution (or 0.5 M KOH) and then immersed in a large amount of water. As shown in Fig. 10b, compared to the original hydrogel, the tensile fracture stress of the reconstructed hydrogel declined from 4.29 to 2.12 MPa, the fracture strain declined from 564% to 321% and the elastic modulus decreased slightly from 16 to 12.8 MPa. After the same hydrogels were reconstructed twice, the tensile fracture stress and fracture strain declined to 1.48 MPa and 257%, respectively, but

the elastic modulus remained unchanged at 12.7 MPa. In order to further study the recycling properties and stability in different environments, the relevant swelling experiment was conducted and the results are shown in Fig. S12a (ESI†), the  $\text{MN}_6$  hydrogel rapidly degraded at pH = 1 or pH > 13, was kept in the primeval state of the swelling equilibrium at pH = 0 and 4–7, and swelled at pH = 2, 10, and 12. We enlarged the swelling curve for the first 7 h in Fig. S12b (ESI†), which more clearly reflects the degradation tendency of the hydrogel at pH = 1. Combined with Fig. S13b (ESI†), we can clearly see that the hydrogel rapidly swelled and degraded within 5 h at pH = 1. The reason for this may be the protonation of the NPAM which resulted in a rapid, thorough break of the hydrogen bonding in the liquid environment at pH = 1. However, at another pH, the protonation or deprotonation of the hydrogel was slow and tended to reach the swelling equilibrium state, therefore it was hard to degrade at another pH. An interesting phenomenon was observed that the hydrogel hardly swelled at pH = 0. Therefore we studied the swelling ratios for the PMAAc hydrogels in Fig. S13a (ESI†), it should be noted that the PMAAc hydrogels also barely swelled at pH = 0. A possible explanation is that the polymer chain could not swell owing to the balance of the internal and external osmotic pressure at pH = 0. To summarize, these hydrogels have the property to degrade rapidly at specific conditions (pH = 1 or pH > 13), which gives efficient and convenient recycling of the hydrogels.

## Conclusions

In summary, a novel tough hydrogen-bonding hydrogel was prepared through the photoinitiated copolymerization of MAAc and NPAM in DMSO and then soaked in water to convert the organogel into a hydrogel. As the viscosity of the organogel shows significant differences at different temperatures and excellent swelling resistance throughout dialysis, we successfully combined a 3D-printing technique with solvent replacement treatment to develop a novel method for fabricating a 3D-printed tough hydrogel. Benefiting from the formation of hydrogen bonding and the stabilization of the hydrophobic interactions, the obtained hydrogel had good mechanical properties. In the absence of any chemical cross-linkers, the hydrogel exhibited an excellent high elastic modulus (up to 66 MPa) and fracture energy (up to  $7.2 \text{ kJ m}^{-2}$ ). Meanwhile, owing to the dynamic nature and temperature sensitivity of the hydrogen bonding, the hydrogel was endowed with fast self-recovery abilities, and thermally activated shape memory properties. Through destroying and reconstructing the hydrogen bonding by changing the pH, the hydrogel demonstrated good recyclability. This hydrogen-bonding hydrogel exhibits 3D printing processability, excellent mechanical properties, good shape memory performance and recyclability, which are desirable for promoting the practical applications of structural biomaterials and environmentally friendly materials, and to facilitate multifunctional hydrogel development.

## Conflicts of interest

There are no conflicts to declare.

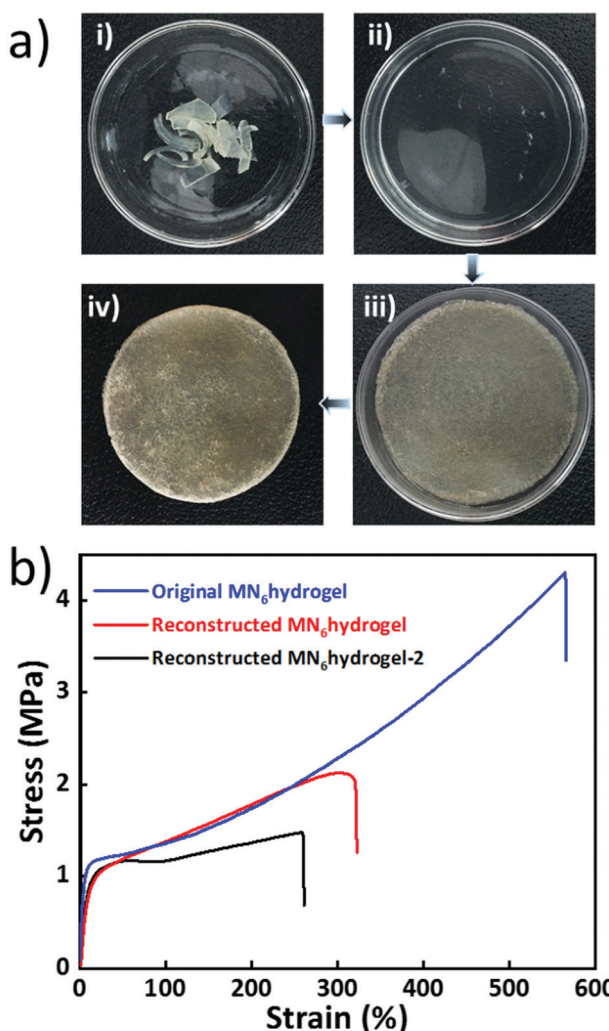


Fig. 10 (a) Reconstruction of the hydrogel film by dissolving the fragments of (i)  $\text{MN}_6$  hydrogel in (ii) 0.5 M KOH solution, (iii) casting into a film, and then (iv) sequential swelling in 0.1 M HCl solution and pure water. (b) Tensile stress-curves of the original, reconstructed  $\text{MN}_6$  hydrogels, and the same hydrogels reconstructed twice.

## Acknowledgements

This work was supported by the National Science Foundation of China (Grant no 51273189), the National Science and Technology Major Project of the Ministry of Science and Technology of China (2016ZX05016), and the National Science and Technology of China (2016ZX05046).

## Notes and references

- 1 C. Ma, T. Li, Q. Zhao, X. Yang, J. Wu, Y. Luo and T. Xie, *Adv. Mater.*, 2014, **26**, 5665–5669.
- 2 C. Ma, W. Lu, X. Yang, J. He, X. Le, L. Wang, J. Zhang, M. J. Serpe, Y. Huang and T. Chen, *Adv. Funct. Mater.*, 2017, 1704568.
- 3 L. Han, X. Lu, M. Wang, D. Gan, W. Deng, K. Wang, L. Fang, K. Liu, C. W. Chan, Y. Tang, L. T. Weng and H. Yuan, *Small*, 2017, **13**, 1601916.
- 4 L. Han, L. Yan, M. Wang, K. Wang, L. Fang, J. Zhou, J. Fang, F. Ren and X. Lu, *Chem. Mater.*, 2018, **30**, 5561–5572.
- 5 B. Xu, Y. Li, F. Gao, X. Zhai, M. Sun, W. Lu, Z. Cao and W. Liu, *ACS Appl. Mater. Interfaces*, 2015, **7**, 16865–16872.
- 6 C. Ghobril and M. W. Grinstaff, *Chem. Soc. Rev.*, 2015, **44**, 1820–1835.
- 7 M. S. Mannoor, Z. Jiang, T. James, Y. L. Kong, K. A. Malatesta, W. O. Soboyejo, N. Verma, D. H. Gracias and M. C. McAlpine, *Nano Lett.*, 2013, **13**, 2634–2639.
- 8 B. Duan, L. A. Hockaday, K. H. Kang and J. T. Butcher, *J. Biomed. Mater. Res., Part A*, 2013, **101**, 1255–1264.
- 9 M. Zarek, M. Layani, I. Cooperstein, E. Sachyani, D. Cohn and S. Magdassi, *Adv. Mater.*, 2016, **28**, 4449–4454.
- 10 J. L. Erkal, A. Selimovic, B. C. Gross, S. Y. Lockwood, E. L. Walton, S. McNamara, R. S. Martin and D. M. Spence, *Lab Chip*, 2014, **14**, 2023–2032.
- 11 X. Zheng, H. Lee, T. H. Weisgraber, M. Shusteff, J. DeOtte, E. B. Duoss, J. D. Kuntz, M. M. Biener, Q. Ge and J. A. Jackson, *Science*, 2014, **344**, 1373–1377.
- 12 J. L. Connell, E. T. Ritschdorff, M. Whiteley and J. B. Shear, *Proc. Natl. Acad. Sci. U. S. A.*, 2013, **110**, 18380–18385.
- 13 J. Odent, T. J. Wallin, W. Pan, K. Kruempelstaedter, R. F. Shepherd and E. P. Giannelis, *Adv. Funct. Mater.*, 2017, **27**, 1701807.
- 14 Z. Xiong, M.-L. Zheng, X.-Z. Dong, W.-Q. Chen, F. Jin, Z.-S. Zhao and X.-M. Duan, *Soft Matter*, 2011, **7**, 10353–10359.
- 15 J. F. Xing, M. L. Zheng and X. M. Duan, *Chem. Soc. Rev.*, 2015, **44**, 5031–5039.
- 16 K. Tian, J. Bae, S. E. Bakarich, C. Yang, R. D. Gately, G. M. Spinks, M. In Het Panhuis, Z. Suo and J. J. Vlassak, *Adv. Mater.*, 2017, **29**, 1604827.
- 17 Z. Chen, D. Zhao, B. Liu, G. Nian, X. Li, J. Yin, S. Qu and W. Yang, *Adv. Funct. Mater.*, 2019, **29**, 1900971.
- 18 S. Wei, G. Qu, G. Luo, Y. Huang, H. Zhang, X. Zhou, L. Wang, Z. Liu and T. Kong, *ACS Appl. Mater. Interfaces*, 2018, **10**, 11204–11212.
- 19 F. Gao, Z. Xu, Q. Liang, B. Liu, H. Li, Y. Wu, Y. Zhang, Z. Lin, M. Wu, C. Ruan and W. Liu, *Adv. Funct. Mater.*, 2018, **28**, 1706644.
- 20 X. Li, H. Wang, D. Li, S. Long, G. Zhang and Z. Wu, *ACS Appl. Mater. Interfaces*, 2018, **10**, 31198–31207.
- 21 R. L. Truby and J. A. Lewis, *Nature*, 2016, **540**, 371–378.
- 22 S. E. Bakarich, M. I. H. Panhuis, S. Beirne, G. G. Wallace and G. M. Spinks, *J. Mater. Chem. B*, 2013, **1**, 4939–4946.
- 23 S. E. Bakarich, P. Balding, R. Gorkin III, G. M. Spinks and M. In het Panhuis, *RSC Adv.*, 2014, **4**, 38088–38092.
- 24 F. Zhu, L. Cheng, J. Yin, Z. L. Wu, J. Qian, J. Fu and Q. Zheng, *ACS Appl. Mater. Interfaces*, 2016, **8**, 31304–31310.
- 25 S. Hong, D. Sycks, H. F. Chan, S. Lin, G. P. Lopez, F. Guilak, K. W. Leong and X. Zhao, *Adv. Mater.*, 2015, **27**, 4035–4040.
- 26 X. Kuang, K. Chen, C. K. Dunn, J. Wu, V. C. F. Li and H. J. Qi, *ACS Appl. Mater. Interfaces*, 2018, **10**, 7381–7388.
- 27 A. Kirillova, R. Maxson, G. Stoychev, C. T. Gomillion and L. Ionov, *Adv. Mater.*, 2017, **29**, 1703443.
- 28 T. Nakajima, H. Sato, Y. Zhao, S. Kawahara, T. Kurokawa, K. Sugahara and J. P. Gong, *Adv. Funct. Mater.*, 2012, **22**, 4426–4432.
- 29 J. P. Gong, *Soft Matter*, 2010, **6**, 2583–2590.
- 30 F. Luo, T. L. Sun, T. Nakajima, T. Kurokawa, Y. Zhao, K. Sato, A. B. Ihsan, X. Li, H. Guo and J. P. Gong, *Adv. Mater.*, 2015, **27**, 2722–2727.
- 31 T. Nakajima, Y. Fukuda, T. Kurokawa, T. Sakai, U.-I. Chung and J. P. Gong, *ACS Macro Lett.*, 2013, **2**, 518–521.
- 32 L. Agüero, L. G. Guerrero-Ramírez and I. Katime, *Mater. Sci. Appl.*, 2010, **01**, 103–108.
- 33 X. Dai, Y. Zhang, L. Gao, T. Bai, W. Wang, Y. Cui and W. Liu, *Adv. Mater.*, 2015, **27**, 3566–3571.
- 34 L. Tang, W. Liu and G. Liu, *Adv. Mater.*, 2010, **22**, 2652–2656.
- 35 H. Miyaji, M. Dudic, J. H. Tucker, I. Prokes, M. E. Light, M. B. Hursthouse, I. Stibor and P. Lhoták, *Tetrahedron Lett.*, 2002, **43**, 873–878.
- 36 J. Steinke, I. Dunkin and D. Sherrington, *TrAC, Trends Anal. Chem.*, 1999, **18**, 159–164.
- 37 A. T. A. Mubarak, A. Z. El-Sonbati and A. A. El-Binary, *Appl. Organomet. Chem.*, 2004, **18**, 212–220.
- 38 L. Guo, H. Sato, T. Hashimoto and Y. Ozaki, *Macromolecules*, 2010, **43**, 3897–3902.
- 39 M. Guo, L. M. Pitet, H. M. Wyss, M. Vos, P. Y. Dankers and E. Meijer, *J. Am. Chem. Soc.*, 2014, **136**, 6969–6977.
- 40 X. Hu, M. Vatankhah-Varnoosfaderani, J. Zhou, Q. Li and S. S. Sheiko, *Adv. Mater.*, 2015, **27**, 6899–6905.
- 41 Y. Zhang, Y. Li and W. Liu, *Adv. Funct. Mater.*, 2015, **25**, 471–480.
- 42 T. J. Wallin, J. Pikul and R. F. Shepherd, *Nat. Rev. Mater.*, 2018, **3**, 84–100.
- 43 K. J. Henderson and K. R. Shull, *Macromolecules*, 2012, **45**, 1631–1635.
- 44 G. Song, L. Zhang, C. He, D.-C. Fang, P. G. Whitten and H. Wang, *Macromolecules*, 2013, **46**, 7423–7435.
- 45 C. Xu, Q. Tang, H. Yang, K. Peng and X. Zhang, *Macromol. Chem. Phys.*, 2018, **219**, 1700636.
- 46 W. Feng, W. Zhou, Z. Dai, A. Yasin and H. Yang, *J. Mater. Chem. B*, 2016, **4**, 1924–1931.